Applied Catalysis B: Environment and Energy 347 (2024) 123770

Contents lists available at ScienceDirect

Applied Catalysis B: Environment and Energy

journal homepage: www.elsevier.com/locate/apcatb

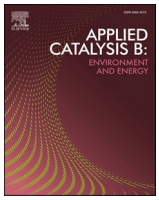

Layered charge separation in surface boron doped copper with phosphate groups boosts the electrochemical uranium extraction from seawater

Jiejie Li [1,a], Chi Jiao [1,b], Yang Lin [a], Yuanhao Li [a], Zishu Qian [a], Huanhuan Liu [a], Tao Chen [a], Yan Liu [b,*], Rong He [a,*], Wenkun Zhu [a,*]

[a] State Key Laboratory of Environment-friendly Energy Materials, National Co-innovation Center for Nuclear Waste Disposal and Environmental Safety, Nuclear Waste and Environmental Safety Key Laboratory of Defense, School of National Defense of Science and Technology, Southwest University of Science and Technology, Mianyang 621010, China

[b] School of Chemistry and Materials Science, Anhui Normal University, Wuhu 241002, Anhui, China

ARTICLE INFO

Keywords:
Electrochemical uranium extraction
Seawater
Uranyl binding
Charge separation

ABSTRACT

Electrochemical uranium extraction from seawater is an attractive project for sustainable nuclear industry, whereas the active sites of electrode materials require further promotion on uranyl binding to increase the efficiency and kinetics of uranium extraction. Herein, we construct a strategy of layered charge separation in surface boron-doped copper with surface phosphate ions (B:Cu-PO_4) for charge-enhanced uranyl binding and extraction in seawater. The B atoms were demonstrated to decrease the negative charge in surface Cu atoms and increase the negative charge in outer O atoms of PO_4^{3-} groups, thus enhancing the uranyl binding. In a real seawater experiment, the B:Cu-PO_4 extracted 24.9 μg of uranium from 10 L of seawater. Such performance corresponded to a considerable extraction capacity of 2.1 mg/g per day, which outperformed most of the state-of-the-art materials. The successful construction of charge separation in B:Cu-PO_4 broadened the material design for uranium extraction from real seawater.

1. Introduction

The development of the nuclear industry has induced the mass consumption of uranium resources, which is predicted to be exhausted in terrestrial ores within one century [1,2]. Due to the approximately 45 billion tons of uranium in the ocean, the uranium extraction in seawater is particularly appealing for affording nuclear development for thousands of years [3–6]. The traditional adsorption method for uranium extraction in seawater suffers from sluggish kinetics and low extraction capacity in the complex environment of real seawater [7–11]. As an alternative to the adsorption method, the electrochemical uranium extraction method can reduce uranyl ions in seawater to insoluble species. This method possesses several advantages, such as rapid kinetics driven by the electric field, enhanced resistance for non-reductive interfering ions, and promoted extraction capacity induced by the crystallization of the final uranium products [12–14]. In electrochemical uranium extraction, the efficiency mainly depends on the electrode materials, which motivates the researchers to explore the rational design of materials[15–17].

Typically, the electrode materials for electrochemical uranium extraction possess high conductivity and specific sites for the binding of uranyl (UO_2^{2+}). The two factors respectively ensure the activity of electrochemical reaction and the selectivity for uranium extraction. For example, Fe-N-C single atoms on conductive carbon support were coupled with amidoxime binding sites, which achieved 1.2 mg/g of extraction capacity within 24 h towards electrochemical uranium extraction in real seawater [18]. As another example, bovine serum albumin coated carbon fiber felts were reported to possess 0.37 mg/g per day of extraction capacity, with carbon fiber as conductive support and oxygenic functional groups as specific sites [19]. Despite the progress, the efficiency and kinetics of uranium extraction were still unsatisfied because of the complex environment in real seawater, which drives the further promotion of active sites for uranyl binding [20–22].

A promising approach to enhance the uranyl binding and reduction is the engineering spatial distribution of charge in the active sites [23]. Considering the electronic structure of uranyl, a stable binding structure requires the negative charge of the active center with the binding of U atom in uranyl, together with the positive charge of another center with

* Corresponding authors.
E-mail addresses: ly0201@ahnu.edu.cn (Y. Liu), her@swust.edu.cn (R. He), zhuwenkun@swust.edu.cn (W. Zhu).
[1] These authors contributed equally to this work.

https://doi.org/10.1016/j.apcatb.2024.123770
Received 25 October 2023; Received in revised form 29 December 2023; Accepted 21 January 2024
Available online 24 January 2024

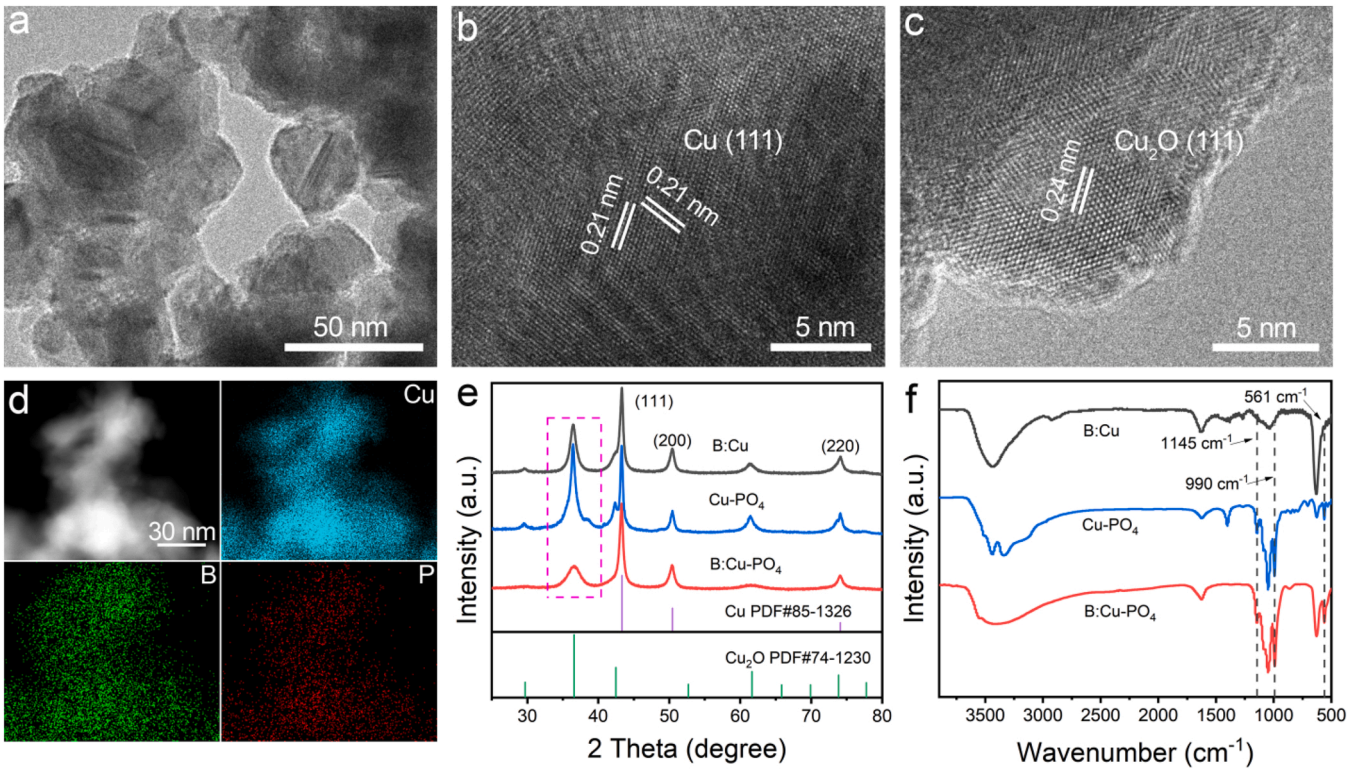

Fig. 1. TEM (a), HRTEM (b and c), and EDS elemental mapping (d) images of B:Cu-PO_4 nanoparticle; (e) XRD patterns of B:Cu, Cu-PO_4, and B:Cu-PO_4 nanoparticles; (f) FTIR spectra of B:Cu, Cu-PO_4, and B:Cu-PO_4 nanoparticles.

the binding of O atom in the uranyl [24,25]. Therefore, the layered charge separation is highly desired to achieve the charge-enhanced multisite binding of uranyl.

To construct an efficient binding site with layered charge separation for U(VI) binding, we chose surface phosphate ions (PO_4^{3-}) as the basic sites. According to the hard and soft acids and bases theory (HSAB), the PO_4^{3-} group serves as the "hard base" and possessed a strong binding strength for U(VI), which is a "hard acid". Additionally, the PO_4^{3-} group was highly negative charged, which gave a strong Coulomb interaction with U(VI). In common, the PO_4^{3-} group can conjunct with metallic surface through P-O-M (M is metal) bonds and exposed several negative charged O atoms [26]. Serving as the active centers, these O atoms were able to strongly bind with uranyl. In this adsorption model, the charge density of these O atoms can be manipulated by the metal-PO_4^{3-} interface, which directly influences the Coulomb interaction and thus binding strength for U(VI). Therefore, the surface inbuilt electric tuning of PO_4^{3-} group is a potential effective strategy for efficient uranium extraction from seawater.

Herein, we simultaneously introduced interstitial B atoms and surface phosphate ions (PO_4^{3-}) into metallic Cu nanoparticles (B:Cu-PO_4), so as to achieve the layered charge separation in the whole materials and thus enhance the electrochemical uranium extraction from seawater. In this case, due to the differences in electronegativity, the B atoms decreased the negative charge in the outer surface of Cu atoms, which enhanced the bonding for O atoms in uranyl and stabilized the surface PO_4^{3-} sites. Meanwhile, the exposed O atoms in PO_4^{3-} sites possessed the increased negative charge and facilitated the binding with U atoms in uranyl. Taken together, the B:Cu-PO_4 exhibited 2.1 mg/g per day of extraction capacity in real seawater (the mass of extraction materials included the B:Cu-PO_4 and the carbon felt support), which represented a considerable value compared with the state-of-the-art materials. The mechanistic study revealed that the B atoms played an important role in the charge separation and enhanced uranyl binding, thus significantly promoting the uranium extraction performance.

2. Experimental

2.1. Materials

Copper(II) chloride ($CuCl_2$), sodium borohydride ($NaBH_4$), and disodium hydrogen phosphate (Na_2HPO_4) were provided by Sinopharm Chemical Reagent Co., Ltd. Sodium sulfate (Na_2SO_4) and hydrazine hydrate ($N_2H_4{\cdot}H_2O$) were provided by Chengdu Kelong Chemical Co., Ltd. Uranyl nitrate ($UO_2(NO_3)_2{\cdot}6\ H_2O$), carbon (Vulcan xc-72), and arsenazo III were purchased from Shanghai Macklin Biochemical Technology Co., Ltd. All of the chemicals used in this experiment were analytical grade and used without further purification.

2.2. Preparation of B:Cu, Cu-PO_4, B:Cu-PO_4

Briefly, B:Cu and Cu samples were prepared through a simple reduction method using copper(II) chloride ($CuCl_2$), sodium borohydride ($NaBH_4$), and hydrazine hydrate($N_2H_4{\cdot}H_2O$) as precursors. Since boron solubility in copper is low, $CuCl_2$ was added into a highly concentrated sodium borohydride solution instantly in order to alloy the boron with copper as high loading as possible. In detail, the B:Cu sample was prepared by (0.37 M, 2 ml) $CuCl_2$ and (5 M, 2 ml) $NaBH_4$ solutions using frozen deionized water, respectively. Notably, $CuCl_2$ solution was rapidly injected into $NaBH_4$ (5 M, 2 ml) solution in an ice water bath until no bubbles formed. Copper precursors were prepared using $N_2H_4{\cdot}H_2O$ instead of $NaBH_4$ by the same steps as B:Cu samples.

In a synthesis of B:Cu-PO_4 and Cu-PO_4, a solution of disodium hydrogen phosphate (0.085 M 1 ml) was added to B:Cu and Cu where the reaction bubbles disappeared, stirred for 20 min, and then left to stand. The precipitates obtained were subsequently washed with water and acetone to completely remove the unreacted precursors and other possible byproducts. the powder was immediately dried under a vacuum overnight.

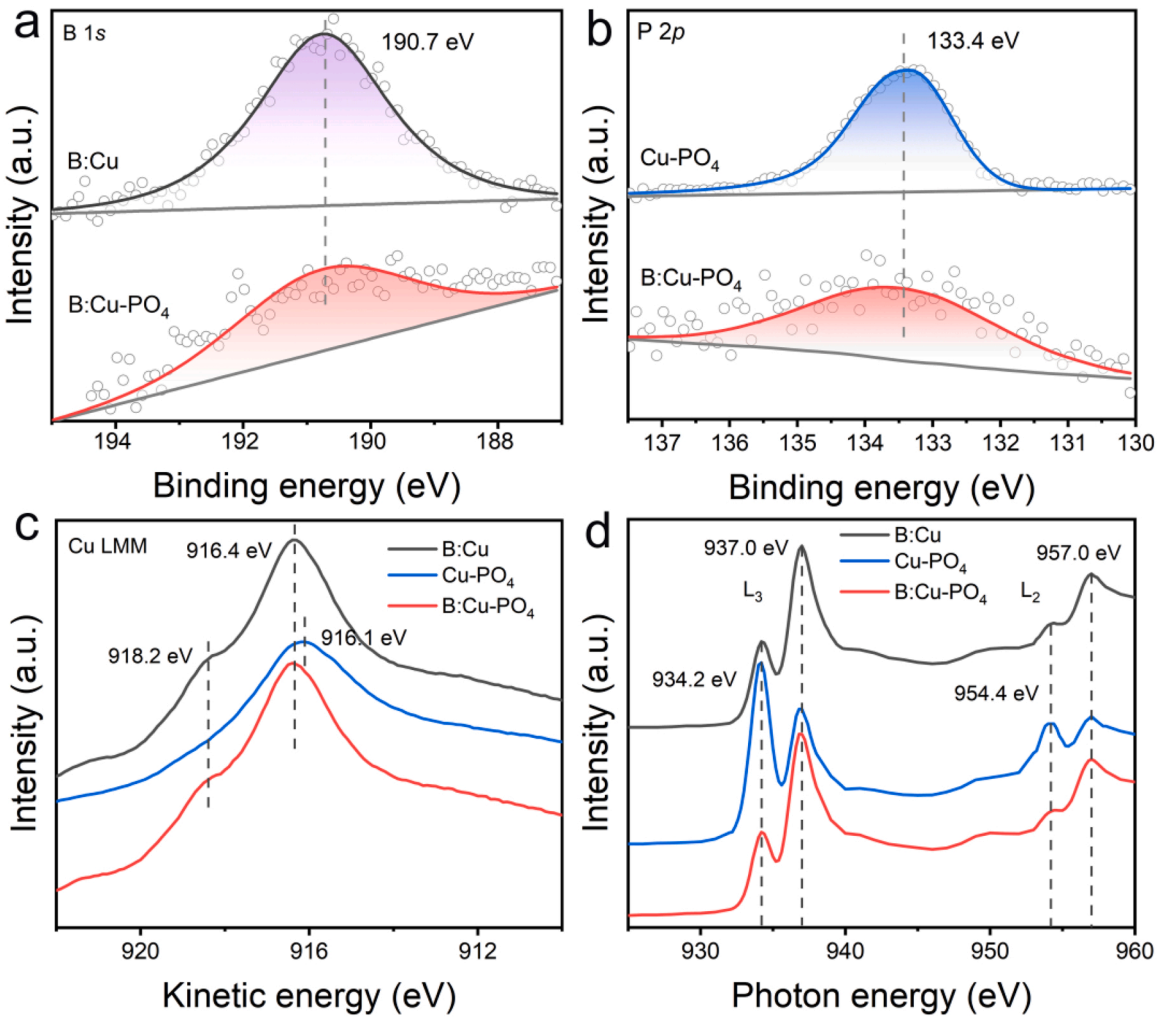

Fig. 2. (a) B 1 *s* XPS spectra of the B:Cu and B:Cu-PO_4 nanoparticles; (b) P 2*p* XPS spectra of the Cu-PO_4 and B:Cu-PO_4 nanoparticles; (c) Cu LMM AES spectra of B:Cu, Cu-PO_4, and B:Cu-PO_4 nanoparticles; (d) Cu L-edge XANES spectra of B:Cu, Cu-PO_4, and B:Cu-PO_4 nanoparticles.

2.3. Characterization

Transmission electron microscopy (TEM) and high-resolution TEM (HRTEM) images were obtained by field-emission high-resolution transmission electron microscopy (FEI Tecnai G2 F20, America FEI). The morphology of the electrocatalysts was explored by Scanning electron microscopy (SEM, JSM-6700 F). X-ray diffraction (XRD) patterns were performed by using a Rigaku Ultma IV Super diffract meter at a scanning speed of 2°/min and a scanning angle of 10–80°. Auger electron spectrometer (AES) and X-ray photoelectron spectroscopy (XPS) measurements were obtained by Thermo Scientific K-Alpha spectrometer using a monochromatic Al Kα source. The Fourier transform infrared (FTIR) spectroscopy was measured by Thermo Scientific Nicolet 6700 Spectrometer. The hydrophilic/hydrophobic properties were performed by measuring the contact angle of water using Chengde Dingsheng JY-82 C Video Contact Angle Tester. Raman spectroscopy (Horiba LabRAM HR Evolution) was collected to further determine the composition of the material. The electrochemical reduction of uranium was measured on an electrochemical station (CHI 660E).

2.4. Electrochemical uranium extraction experiment

Electrochemical uranium extraction was performed with an electrochemical workstation (CHI 660E, China) in a standard three-electrode system. At was used as the counter electrode and Ag/AgCl as the reference electrode in the system. The working electrode was prepared by 5 mg of B:Cu-PO_4 and 3 mg of carbon black dissolved in 2 ml alcohol and 35 μL Nafion solution (5 wt%). Ultrasound until the solute was evenly distributed, and applied it evenly on 1 × 2 cm carbon felt. Removed and used as a working electrode after drying.

3. Results and discussion

To begin with, B:Cu and Cu products were respectively prepared via the reduction of $CuCl_2$ precursor by $NaBH_4$ and N_2H_4, followed by ultrasonic treatment with Na_2HPO_4 to obtain B:Cu-PO_4 and Cu-PO_4. The Scanning electron microscopy (SEM) images indicated a similar nanoparticle of B:Cu, Cu-PO_4, and B:Cu-PO_4 (Fig. S1). As shown by transmission electron microscopy (TEM) images, the nanoparticle was closely stacked in a gel status, which prevented the potential leaching in the electrochemical process (Fig. 1a). In the center region of the gel-like product, the interplanar spacings of lattice fringe in high-resolution TEM (HRTEM) image of B:Cu-PO_4 corresponded to {111} facets of the *fcc*-Cu (0.21 nm), due to the rare alternation of crystal structure by the surface doping of B (Fig. 1b) [27,28]. Moreover, the HRTEM at the edge of the B:Cu-PO_4 product possessed the characteristic lattice fringe of Cu_2O, indicating the surface oxidation (Fig. 1c). By comparison, the oxidation signal appeared in the central region of Cu-PO_4 (Fig. S2). This result proved that the incorporation of B partially increased the anti-oxidation of Cu nanoparticles, which was beneficial to the

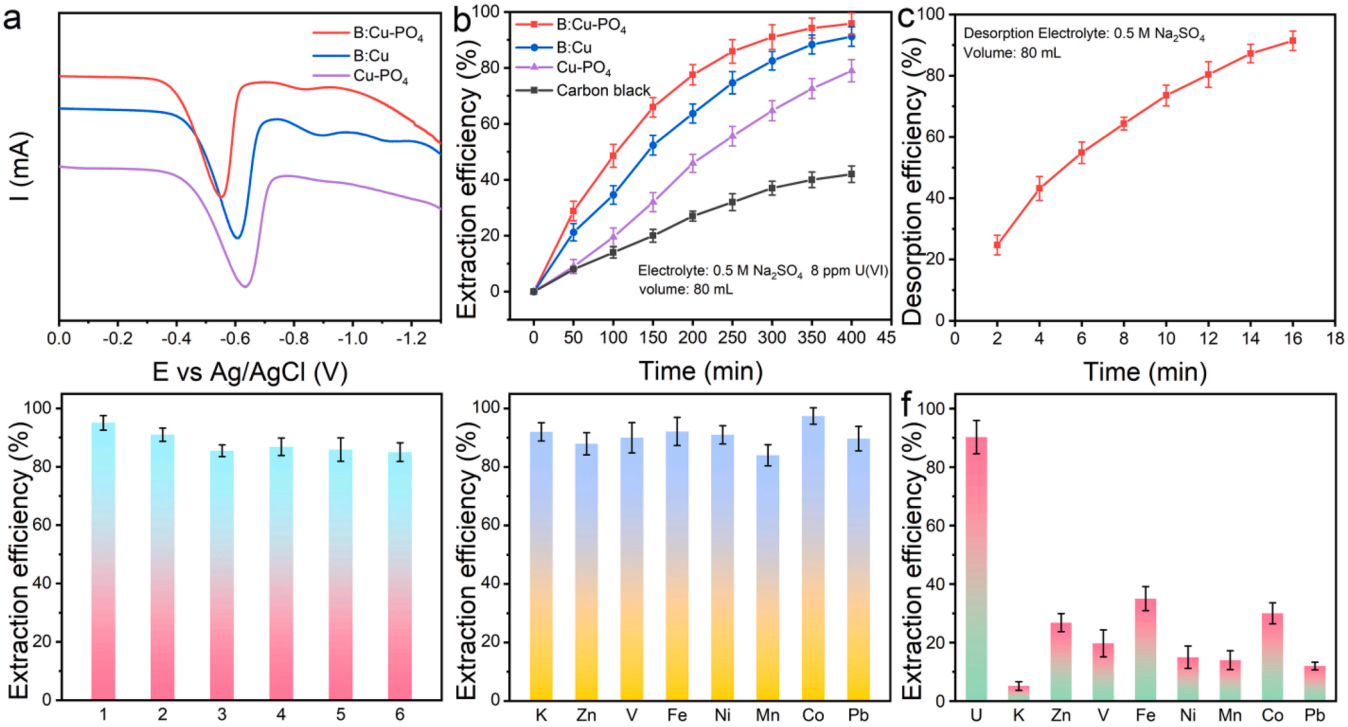

Fig. 3. (a) LSV curves over B:Cu, Cu-PO_4, and B:Cu-PO_4 nanoparticles in the presence of U(VI); (b) Uranium extraction plot versus the contact time in 8 ppm uranium-spiked simulated seawater; (c) The desorption efficiency of B:Cu-PO_4 nanoparticle in 0.5 M of Na_2SO_4 solution; (d) Reusability of B:Cu-PO_4 nanoparticle in 8 ppm uranium-spiked simulated seawater; (e) The extraction efficiency of B:Cu-PO_4 nanoparticle in the presence of individual interfering metal ion in 8 ppm of simulated seawater; (f) Extraction efficiency of uranium and the co-existing metal ion in 8 ppm simulated seawater.

conductivity in the electrochemical application [24]. Due to the gel-like morphology and surface oxidation, the three samples all exhibited the hydrophilicity in static water contact angle test (Fig. S3) [29,30]. Fig. 1d shows the energy dispersive spectroscopy (EDS) mapping of B:Cu-PO_4. The distribution of Cu, B, and P all outlined the B:Cu-PO_4 in the selected region, demonstrating the uniform distribution.

To further investigate the structure of B:Cu-PO_4, we conducted X-ray diffraction (XRD) and Fourier transform infrared (FTIR) measurements. In XRD patterns, both Cu and Cu_2O phases were observed in the B:Cu, Cu-PO_4, and B:Cu-PO_4 samples (Fig. 1e) [31]. Regardless of the B incorporation, the diffraction peak of Cu was located at the same position, which excluded the lattice expansion of lattice doping and verified the surface doping. Additionally, the diffraction peak of Cu_2O in Cu-PO_4 was strongest among the three samples, further demonstrating the stability improvement of Cu by B doping. Fig. 1f shows three new peaks appeared in the FTIR spectra of B:Cu-PO_4 and Cu-PO_4 at 561 cm^{-1}, 990 cm^{-1}, and 1145 cm^{-1}, which can be attributed to the in-side-plane vibration of the phosphate group, the vibration of P-O, and P = O [32–35].

The composition and structure of the B:Cu, Cu-PO_4, and B:Cu-PO_4 nanoparticles were further investigated. As shown in Fig. S4, the peak positions in the Cu 2*p* XPS spectra of B:Cu-PO_4, Cu-PO_4, and B:Cu nanoparticles exhibited similar Cu $2p_{3/2}$ and Cu $2p_{1/2}$ peaks at 932.7 eV and 952.5 eV, respectively [36,37]. Fig. 2a shows the B 1 *s* XPS spectra of the B:Cu and B:Cu-PO_4, the B spectrum consisted of a single peak at 190.7 eV, which was lower than that of B-O bonds (~192 eV) and excluded the surface adsorbed boron oxide. This result indicates that B existed in the form of neutral or negative valence, which was consistent with the Cu-B species induced by B surface doping [26,38]. As shown in Fig. 2b, the P 2*p* peak positions of the Cu-PO_4 and B:Cu-PO_4 samples were located at 133.4 eV, corresponding to the P-O bond. Specially, the B:Cu-PO_4 sample had a wider half-peak width than that of Cu-PO_4, originating from the tuned localized electron density of PO_4 by neighboring B doping [32,39].

We conducted Auger electron spectra (AES) and X-ray adsorption spectra (XAS) to further clarify the electronic structure. As shown by the AES at the Cu LMM region, the dominant peaks of the three samples were all located at 916.1 eV due to surface oxidation (Fig. 2c). However, B:Cu-PO_4 and B:Cu exhibited a more obvious shoulder peak at 918.2 eV relative to Cu-PO_4, which demonstrated an increased percentage of Cu^0 on the surface after the incorporation of B [40]. This result was consistent with the observed oxidation regions in former HRTEM results. Apart from the surface valence, we performed the Cu L-edge X-ray absorption near-edge structure (XANES) measurement to obtain comprehensive information on the electronic state (Fig. 2d). Differential from the overwhelming Cu^+ state at the surface, both Cu L_2 and L_3 edges of the three samples contained two characteristic peaks of Cu^0 (937.0 eV) states, indicating the metallic state of the overall nanoparticles [41,42]. Considering the two peaks at 934.2 eV and 937.0 eV in Cu L_3 edge regions, the peak intensity at 934.2 eV was higher in Cu-PO_4 sample, whereas the opposite results occurred in B:Cu and B:Cu-PO_4 samples. Such a phenomenon resulted from the electron transfer from the Cu atom to the doped B atoms, which gave rise to the increased energy of the electron transition from 1 *s* to 4 *s*. Based on the analysis above, the incorporation of B in B:Cu-PO_4 nanoparticle decreased the surface oxidation and altered the overall electron density of Cu^0, which was potentially beneficial to the electrochemical uranium extraction by promoting the conductivity and manipulating the charge-enhanced uranyl adsorption.

The electrochemical uranium extraction performance of B:Cu-PO_4 nanoparticle was tested in the simulated seawater. At first, we explored the linear sweep voltammetry (LSV) curve in the electrolyte containing 600 ppm U(VI) and 0.5 M Na_2SO_4. Relative to B:Cu and Cu-PO_4, the B:Cu-PO_4 nanoparticles exhibited less negative potential for the reduction peak of U(VI), indicating the introduction of B and PO_4^{3-} facilitated the electrochemical reduction of U(VI) (Fig. 3a). After a continuous electrolysis, the yellow solid was obviously deposited on the electrode, demonstrating the feasibility of electrochemical extraction of U(VI)

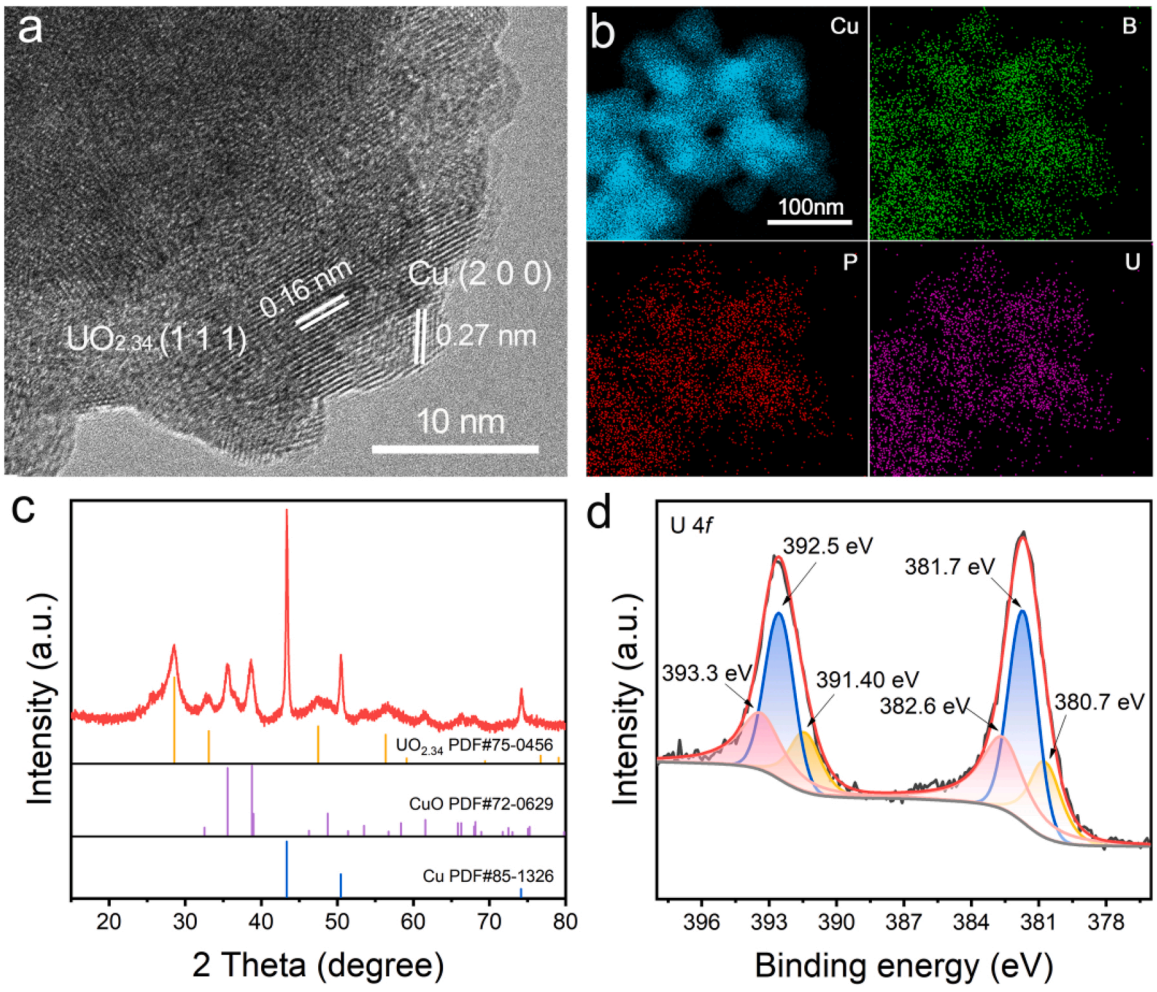

Fig. 4. (a) HRTEM images of Cu-PO_4 nanoparticle after 8 h electrochemical in 8 ppm uranium-simulated seawater; (b) EDS elemental mapping images of the B:Cu-PO_4 nanoparticle after 8 h electrochemical extraction in 8 ppm uranium-spiked seawater; (c) XRD patterns of the B:Cu-PO_4 after the entire uranium extraction; (d) U 4 *f* XPS spectra of the B:Cu-PO_4 nanoparticle after the entire uranium extraction.

(Fig. S5). We then evaluated the electrochemical extraction efficiency of U(VI) for the three samples in simulated seawater (8 ppm U(VI) and 0.5 M Na_2SO_4) at − 1.7 V vs. Ag/AgCl. As shown in Fig. 3b, the B:Cu-PO_4 nanoparticle exhibited a considerable extraction efficiency of 95.8% within 400 min, which outperformed 90.5% of B:Cu and 78.9% of Cu-PO_4. Moreover, the efficiency of uranium extraction by B:Cu-PO_4 is much higher than that of carbon black, which exclude the influence of carbon black on uranium extraction. During the test, B:Cu-PO_4 nanoparticle kept a steady current density of 30 mA/cm^2 (Fig. S6). As shown in Fig. S7, the uranium extraction efficiency of B:Cu-PO_4 was measured in simulated seawater under direct current and pulse current, the extraction efficiency of pulse current was slightly better than direct current, which was attributed to the suppressive hydrogen evolution, as reported by previous literature [12].

To verify the influence of the applied potential, we tested the uranium extraction at − 1.3 V and − 1.5 V vs. Ag/AgCl, which respectively exhibited 57.8% and 77.9% extraction efficiency (Fig. S8). Further decreasing the potential to open the circuit resulted in a dramatic decrease to 5.8% for extraction efficiency of U(VI), demonstrating the key role of electrochemical extraction, rather than physical or chemical adsorption. Meanwhile, the B:Cu-PO_4 nanoparticle displayed a high extraction efficiency regardless of the initial concentration (8, 20, 50 ppm) of U(VI) (Fig. S9). In the desorption part, the extracted U in B:Cu-PO_4 nanoparticle quickly released to the desorption electrolyte with a positive current density of 15 mA/cm^2 in 16 min (Fig. 3c). Through the cycle of electrochemical extraction and desorption, the B:Cu-PO_4 nanoparticle was demonstrated to be stable in 6 cycles, with the persistence of > 85.0% for the extraction efficiency of U(VI) (Fig. 3d). We collected B: Cu-PO_4 material after six cycling for FTIR spectra. As shown in Fig. S10, the stretching vibration peaks appearing at 1145 cm^{-1} and 561 cm^{-1} represented phosphate groups, indicating the stability of PO_4 after cycling. Moreover, the peak at 869 cm^{-1} in the FTIR spectrum was significantly enhanced, which indicated the existence of O═U═O on the surface of the sample. Additionally, we further tested the XPS spectrum. As shown in Fig. S11, the peak located at 134.7 eV, corresponding to P 2*p*. These results demonstrated the remarkable performance of B:Cu-PO_4 nanoparticle for the electrochemical uranium extraction.

In order to investigate the effects of various interfering ions in the ocean on the extraction performance of B:Cu-PO_4 nanoparticle for uranium, we further tested the anti-interference and competitiveness of B:Cu-PO_4 nanoparticle against different cations and anions under the conditions of simulated seawater. As shown in Fig. 3e, the extraction efficiency of U(VI) over B:Cu-PO_4 nanoparticle for uranium was above 84.0% in the presence of a single interfering cation, including K^+, Zn^{2+}, V^{5+}, Fe^{2+}, etc. Moreover, in the presence of a single anionic interfering ion (such as F^-, CO_3^{2-}, Cl^-, etc.), the extraction efficiency of U(VI) over B:Cu-PO_4 nanoparticle exceeded 89.0% (Fig. S12). When the various interfering cation was co-existent in the electrolyte with a similar concentration in the seawater, the extraction efficiency of U(VI) remained at

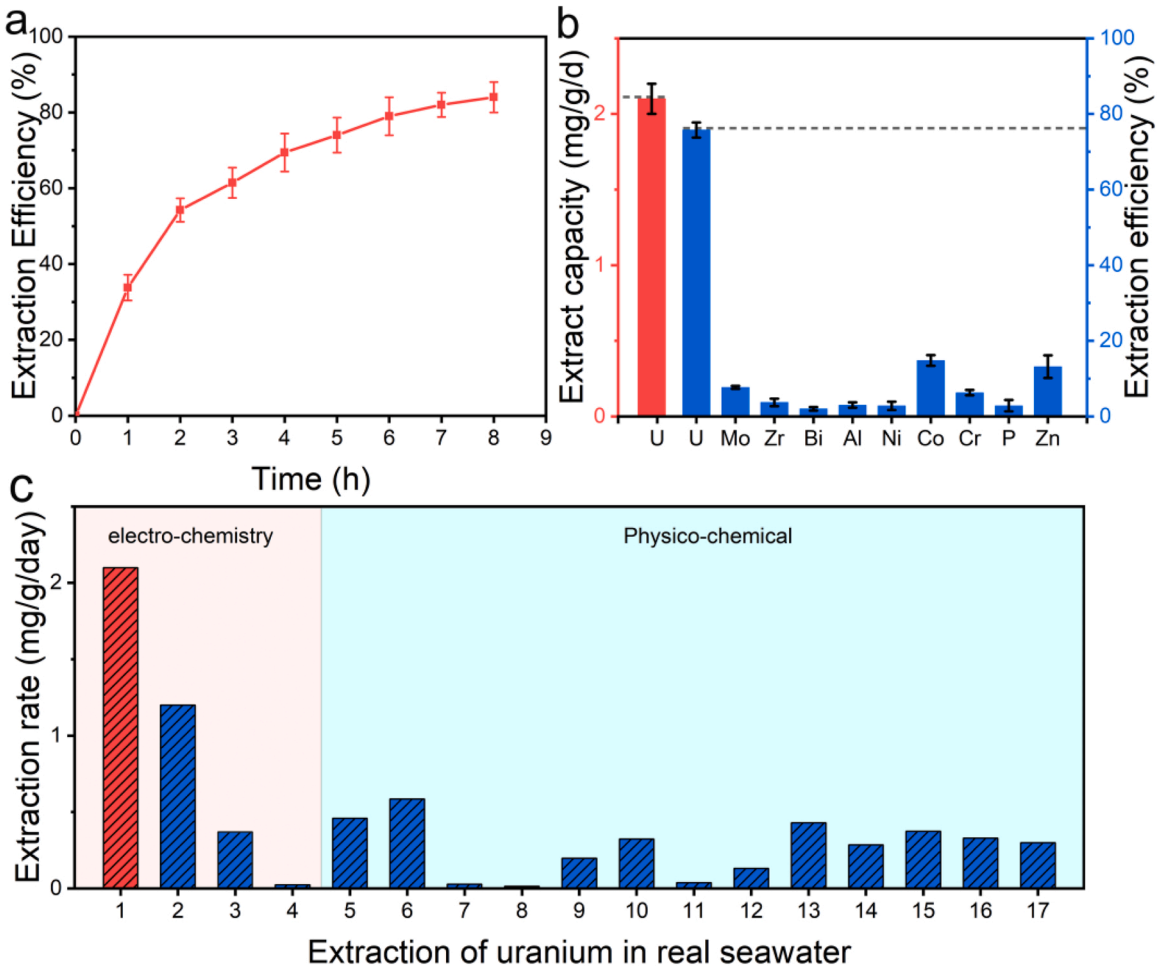

Fig. 5. (a) Uranium extraction plot versus the contact time in 8 ppm uranium-spiked real seawater; (b) The extraction capacity of B:Cu-PO_4 nanoparticle for uranium in real seawater and the extraction efficiency for uranium and other ions; (c) The extraction of uranium compared to other materials. 1 This work, 2 BSA@CFF[19], 3 Fe-N_x-C-R[18], 4 TETA-PAO/GF[44], 5 MUU[45], 6 PAO-OpNpNc[46], 7 PAO-G-A[47], 8 PAO-PNM[48], 9 PAO-Co[49], 10 AOBS-M[50], 11 marine crab carapace [51], 12 CID NFs[52], 13 VA-PG[53], 14 conductive graphene-based PAFs solids[54], 15 PPA@MISS-PAF-A[55], 16 Zn^{2+}-PAO[56], 17 AO-HNTs[57]. The mass of extraction materials included the B:Cu-PO_4 and the carbon felt support.

a high value of 90.3%, whereas the extraction efficiencies of other cations were all lower than 37.0%, indicating the selectivity of U(VI) extraction in seawater over B:Cu-PO_4 nanoparticle (Fig. 3f).

The product of extracting U (VI) from B:Cu-PO_4 nanoparticle was collected to explore the extraction mechanism. Fig. 4a shows the HRTEM image of B:Cu-PO_4 nanoparticle after uranium extraction. The surface of B:Cu-PO_4 nanoparticle tended to be transformed in a disordered lattice, which was attributed to the surface coverage of uranium. In addition, The HRTEM images reveal that the lattice spacing of Cu (2 0 0) and $UO_{2.34}$ (1 1 1) are 0.27 nm and 0.16 nm, which further proves the extraction of uranium. In the elemental mapping, the signal of uranium was uniformly distributed in the selected area, further demonstrating the surface deposition of uranium on B:Cu-PO_4 nanoparticle (Fig. 4b). As shown by XRD pattern of B:Cu-PO_4 nanoparticle after uranium extraction in Fig. 4c, the appearance of the additional distinct diffraction peaks strongly suggested the presence of $UO_{2.34}$ (a special form of UO_{2+x}). This result indicated the crystalline of uranium products were a mix of low-valent uranium and the simultaneous incorporation of U(VI). Such a result was confirmed by the U 4*f* XPS spectrum of B:Cu-PO_4 nanoparticle after uranium extraction (Fig. 4d). The U 4*f* peak was splitted into three peaks at 380.7 eV, 381.7 eV, and 382.6 eV for $4f_{7/2}$, which respectively assigned to U(IV), U(V), and U(VI) species [43]. The various valence of uranium products promoted the formation of insoluble UO_{2+x}.

Based on these findings, we further investigate the potential application of materials in real seawater through electrochemical systems. Through inputting the corresponding concentration of anions and uranium (3.3 μg/L) in Minteq3.0 software, the domain uranium species plotted against pH value was presented in Fig. S13. Considering that the pH in seawater is around 8, the domain species of uranium in seawater is $UO_2(CO_3)_3^{4-}$, which was a typical uranyl complex. To gain a desired extraction efficiency of uranium in seawater, the active sites require the competitive binding for uranyl relative to the CO_3^{2-}, which further drove the design of inbuilt electric tuning. The uranium extraction efficiency was first tested in uranium-spiked real seawater. As shown in Fig. 5a, the uranium extraction efficiency of U(VI) was 84.0% over B:Cu-PO_4 nanoparticle in 8 ppm uranium-spiked real seawater. We then tested the electrochemical uranium extraction over B:Cu-PO_4 nanoparticle in 10 L real seawater without the addition of uranium (3.3 ppb) (Fig. 5b). The efficiency of electrochemical extraction of uranium in 10 L seawater was 75.7% and the extraction capacity was 24.9 μg within 8 h, with a calculated extraction amount of 2.1 mg/g per day. Compared with the state-of-the-art materials in recently reported literature, our performance represented a high level of extraction capacity per day, indicating extraordinary extraction efficiency and kinetics (Fig. 5c) [18,19,44–57]. As a result, the B:Cu-PO_4 nanoparticle exhibited the potential ability for electrochemical uranium extraction from real seawater.

The remarkable performance of uranium extraction over B:Cu-PO_4

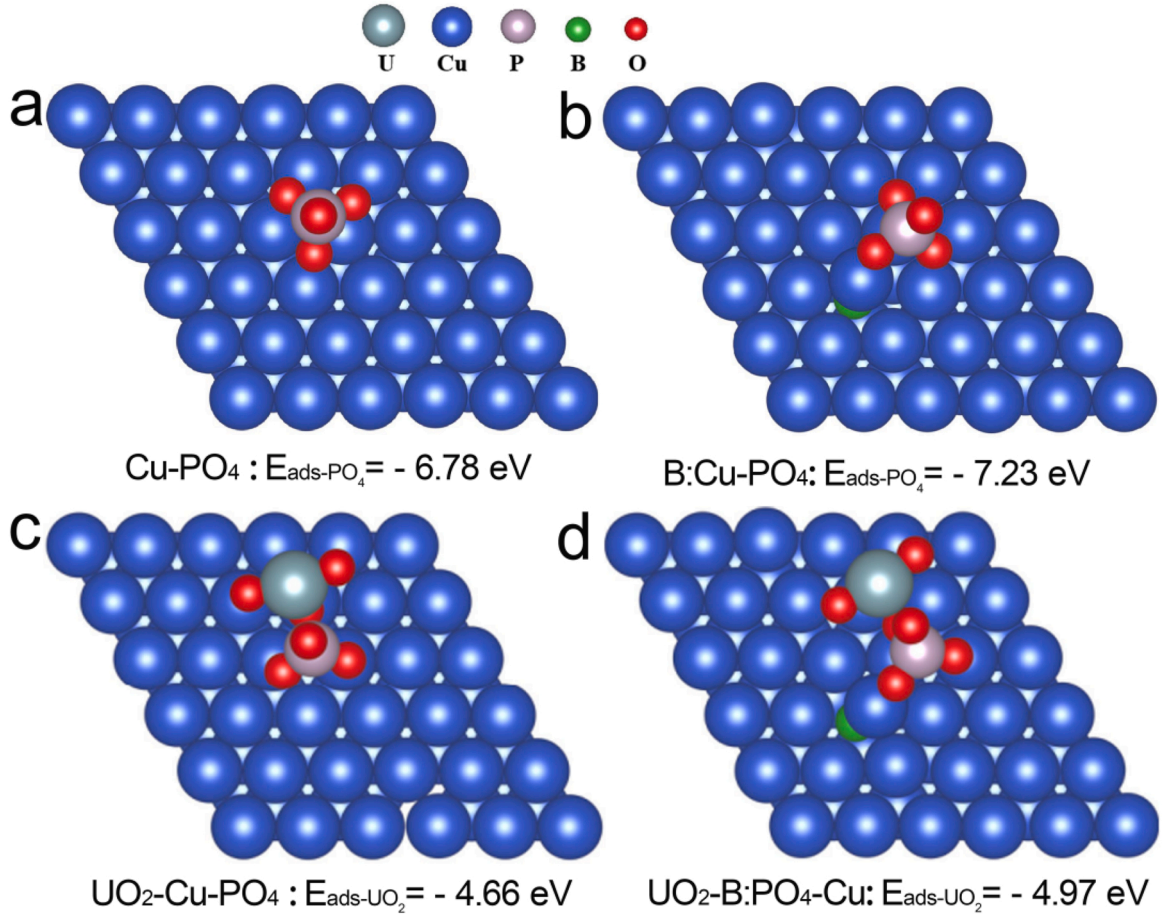

Fig. 6. (a and b) Optimized adsorption configurations of PO_4 adsorbed on the Cu and B:Cu; (c and d) Optimized adsorption configurations of UO_2 adsorbed on the Cu-PO_4 and B:Cu-PO_4. Grey depicts the uranium atom, blue is the copper atom, purple is the phosphorus atom, green is the boron atom, and red is the oxygen atom.

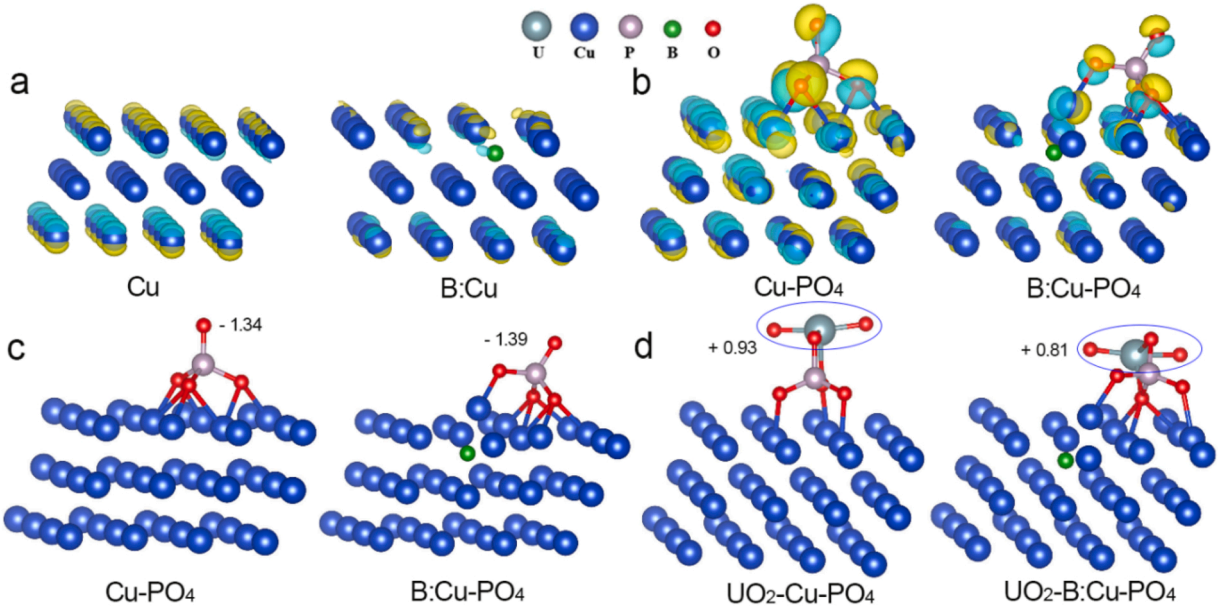

Fig. 7. (a) Differential charge diagram of Cu and B:Cu before and after injection of additional electrons; (b) Differential charge diagram of Cu-PO_4 and B:Cu-PO_4 before and after injection of additional electrons; (c) Charge distribution of Cu-PO_4 and B:Cu-PO_4 before and after injecting additional electrons; (d) Charge distribution of UO_2-Cu-PO_4 and UO_2-B:Cu-PO_4 before and after injecting additional electrons. "+ " represents the electrons obtained from surrounding atoms (resulting in electrons), and "-" denotes the transfer of electrons to surrounding atoms (electron loss). The yellow area represents negative charge, and the green area represents positive charge in the differential charge diagram.

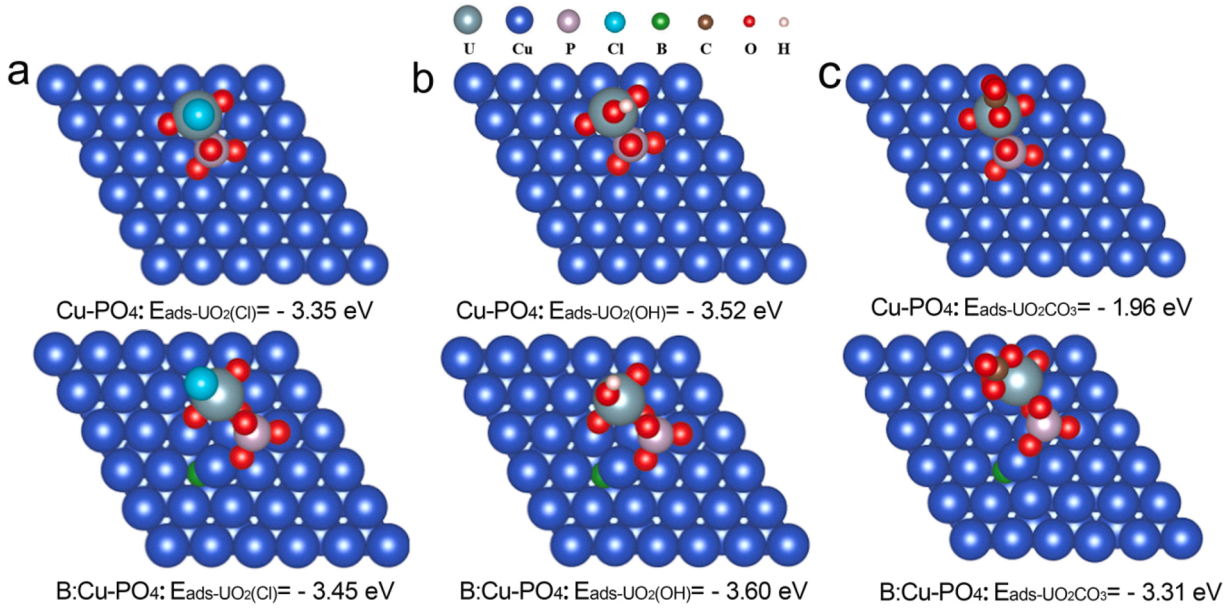

Fig. 8. (a) Optimized adsorption configurations of $[UO_2(CO_3)]$ adsorbed on the Cu-PO_4 and B:Cu-PO_4; (b) Optimized adsorption configurations of $[UO_2(OH)]$ adsorbed on the Cu-PO_4 and B:Cu-PO_4; (c) Optimized adsorption configurations of $[UO_2(Cl)]$ adsorbed on the Cu-PO_4 and B:Cu-PO_4. Grey depicts the uranium atom, blue is the copper atom, purple is the phosphorus atom, light blue represents chlorine atom, green is the boron atom, red is the oxygen atom, grey depicts the uranium atom, blue is the copper atom, purple is the phosphorus atom, green is the boron atom, brown represents carbon atom, red is the oxygen atom, and pink represents hydrogen atom.

nanoparticle motivates us to explore the effect of B and PO_4^{3-} group by theoretical calculations. We calculated the bond length and bond angle of uranyl on Cu-PO_4 and B:Cu-PO_4 in DFT calculations. As shown in Table S1, the difference in bond length and bond angle between B:Cu-PO_4 and Cu-PO_4 is relatively small, which originated from the layered charge separation and verifies the difference in adsorption energy. Fig. 6a and b show the optimized structure of a PO_4^{3-} group adsorbed on Cu and B:Cu slabs, respectively. In the case of B:Cu, the PO_4^{3-} group tended to locate at the Cu atoms which neighbored with B atoms, with an adsorption energy of − 7.23 eV. Such value was more negative than that of the PO_4^{3-} group on the Cu slab, indicating the incorporation of B improved the surface stability of the PO_4^{3-} group, which was beneficial to the persistence of the active sites for uranium extraction [58]. Meanwhile, we calculated the adsorption energy of a uranyl on the Cu-PO_4 and B:Cu-PO_4 slabs, as indicated in Fig. 6c and d. The adsorption energy of uranyl on B:Cu-PO_4 slab was − 4.97 eV, which was more negative than that on Cu-PO_4 slab (−4.66 eV). Both the stability of PO_4^{3-} group and the enhanced adsorption of uranyl on PO_4^{3-} group resulted in the promoted uranium extraction of B:Cu-PO_4.

To further consider the electrochemical environment, we performed the analysis of electronic structure with the injection of additional electrons. Fig. 7a shows the differential charge maps after the electron injection in Cu and B:Cu slabs. The presence of B atom broke the charge symmetry of Cu atoms, resulting in the decreased negative charge on the outer surface of Cu atoms which neighbored with B atom [59]. This result was responsible for the enhanced stability of the surface adsorbed PO_4^{3-} active sites. After the introduction of PO_4^{3-}, the separation of charge on B:Cu-PO_4 slab was more obvious than that on PO_4-Cu slab, together with the exposure of negative charge on the outer O atom in PO_4^{3-} group (Fig. 7b). To verify this point, we marked the Bader charge values of the outer O atom in PO_4^{3-} group (Fig. 7c). The outer O atom in B:Cu-PO_4 slab attained the charge of − 1.39 |e|, which was more negative than − 1.34 |e| of PO_4-Cu slab. Considering the positive nature of uranyl, the PO_4^{3-} group on the B:Cu-PO_4 slab was more active for the uranyl adsorption than the PO_4^{3-} group on the Cu-PO_4 slab. After the adsorption of uranyl, the charges on the outer O atoms of Cu-PO_4 and B:Cu-PO_4 were similar, whereas the overall charge of adsorbed uranyl on B:Cu-PO_4 was less positive than that on Cu-PO_4 (0.81 |e| vs. 0.93 |e|, Fig. 7d). This result demonstrated the enhanced electron transfer from PO_4^{3-} group to adsorbed uranyl after the incorporation of B, which served as the intrinsic factor for the promoted uranium binding.

Additionally, we provided the modified adsorption models that considering ligands of Cl^-, CO_3^{2-}, OH^-, which were widely existed in real seawater. Due to the alkalinity of seawater, the concern on OH^- ligand was recognized as the influence of water. For the ligands of Cl^- and OH^-, the B:Cu-PO_4 with layered charge separation exhibited the adsorption energy of − 3.45 eV and − 3.60 eV, which were more negative than that of Cu-PO_4 (Fig. 8a and b). Notably, for the domain ligand of CO_3^{2-} in seawater, the adsorption energy of UO_2CO_3 was − 3.31 eV on B:Cu-PO_4, which was much more negative than that on Cu-PO_4 (Fig. 8c). Therefore, the layered charge separation strategy was widely effective considering the ligands, especially the ligand of CO_3^{2-} in seawater.

4. Conclusion

In summary, we constructed B:Cu-PO_4 with spatial layered charge separation for boosting the electrochemical uranium extraction from seawater. The introduction of B atoms dramatically increased the kinetics and capacity of uranium extraction, resulting in a remarkable extraction efficiency of 95.8% within 400 min for B:Cu-PO_4 in simulated seawater. In the real seawater experiment, B:Cu-PO_4 exhibited an extraction capacity of 2.1 mg/g per day, which outperformed most of the state-of-the-art materials. The mechanistic study revealed that the B atoms decreased the negative charge in surface Cu atoms and increased the negative charge in outer O atoms of PO_4^{3-} groups, thereby promoting the uranyl binding through enhanced O-Cu and U-O interactions. Our work not only developed a new material for efficient uranium extraction but provided a constructive strategy of layered charge separation for uranyl binding and uranium extraction from real seawater.

CRediT authorship contribution statement

Li Jiejie: Conceptualization, Data curation, Methodology, Writing – original draft. **Liu Yan:** Software, Writing – review & editing. **Chen Tao:**

Writing – review & editing. **Zhu Wenkun:** Project administration. **He Rong:** Conceptualization, Resources, Supervision, Writing – review & editing. **Li Yuanhao:** Data curation, Validation. **Lin Yang:** Conceptualization, Validation. **Liu Huanhuan:** Writing – review & editing. **Qian Zishu:** Investigation. **Jiao Chi:** Formal analysis, Software.

Declaration of Competing Interest

The authors declare that they have no known competing financial interests or personal relationships that could have appeared to influence the work reported in this paper.

Data availability

The authors do not have permission to share data.

Acknowledgment

This work was supported by NSFC (No. 21976147, 21906154 and 22303002), Sichuan Science and Technology Program (No. 2021JDRC0109, 2022JDRC0074, and 2022YFG0371), the Project of State Key Laboratory of Environment-friendly Energy Materials in SWUST (No. 20fksy19), Open Fund of CNNC Key Laboratory for Uranium Extraction from Seawater (KLUES202201). Numerical computations were performed on Hefei advanced computing center.

Appendix A. Supporting information

Supplementary data associated with this article can be found in the online version at doi:10.1016/j.apcatb.2024.123770.

References

[1] S. Kushwaha, K. Patel, Catalyst: uranium extraction from seawater, a paradigm shift in resource recovery, Chem 7 (2021) 271–274.
[2] Anonymous, Nuclear secrets revealed in making light of uranium, Nature 592 (2021), 662-662.
[3] Y. Xie, Z. Liu, Y. Geng, H. Li, N. Wang, Y. Song, X. Wang, J. Chen, J. Wang, S. Ma, G. Ye, Uranium extraction from seawater: material design, emerging technologies and marine engineering, Chem. Soc. Rev. 52 (2023) 97–162.
[4] Y. Li, Y. Zheng, Z. Ahamd, L. Zhu, J. Yang, J. Chen, Z. Zhang, Strategies for designing highly efficient adsorbents to capture uranium from seawater, Coord. Chem. Rev. 491 (2023) 215234.
[5] Y. Wu, Y. Xie, Functional nanomaterials for selective uranium recovery from seawater: Material design, extraction properties and mechanisms, Coord. Chem. Rev. 483 (2023) 215097.
[6] A. Wiechert, S. Yiacoumi, C. Tsouris, The ocean's nuclear energy reserve, Nat. Sustain. 5 (2022) 13–14.
[7] Y. Wu, W. Cui, C. Zhang, R. Liang, J. Qiu, Regenerable, anti-biofouling covalent organic frameworks for monitoring and extraction of uranium from seawater, Environ. Chem. Lett. 19 (2021) 1847–1856.
[8] W. Wang, Q. Luo, J. Li, Y. Li, R. Wu, Y. Li, X. Hu, N. Wang, Single-atom tungsten engineering of MOFs with biomimetic antibiofilm activity toward robust uranium extraction from seawater, Chem. Eng. J. 431 (2022) 133483.
[9] J. Yu, H. Zhang, Q. Liu, J. Yu, J. Zhu, R. Li, P. Liu, Y. Li, J. Wang, Antibacterial AO-CS/CdS-porous few-layer g-C_3N_4 nanofiber membrane for high-efficiency uranium extraction from seawater: a dual adsorption-photocatalytic regulation strategy, Chem. Eng. J. 471 (2023) 144705.
[10] Y. Xu, J. Yu, J. Zhu, Q. Liu, H. Zhang, J. Liu, R. Chen, Y. Li, J. Wang, Cyclized polyacrylonitrile amidoxime with local conjugate domain for high-efficiency extraction of uranium from seawater, Appl. Catal. B Environ. 316 (2022) 121677.
[11] N. Shi, J. Wu, X. Zhi, N. Li, Z. Wang, Amidoxime-functionalized cellulose nanofibers/MXene aerogel for electric field enhanced uranium extraction from seawater, Chem. Eng. J. 476 (2023) 146563.
[12] C. Liu, P. Hsu, J. Xie, J. Zhao, T. Wu, H. Wang, W. Liu, J. Zhang, S. Chu, Y. Cui, A half-wave rectified alternating current electrochemical method for uranium extraction from seawater, Nat. Energy 2 (2017) 17007.
[13] C. Tsouris, Uranium extraction: fuel from seawater, Nat. Energy 2 (2017) 17022.
[14] H. Yang, Y. Liu, Z. Chen, G. Waterhouse, S. Ma, X. Wang, Emerging technologies for uranium extraction from seawater, Sci. China Chem. 65 (2022) 2335–2337.
[15] C. Wang, A. Helal, Z. Wang, J. Zhou, X. Yao, Z. Shi, Y. Ren, J. Lee, J. Chang, B. Fugetsu, J. Li, Uranium in situ electrolytic deposition with a reusable functional graphene-foam electrode, Adv. Mater. 33 (2021) 2102633.
[16] Y. Wang, Y. Wang, M. Song, S. Chen, J. Wei, J. You, B. Zhou, S. Wang, Electrochemical-mediated regenerable Fe^{II} active sites for efficient uranium extraction at ultra-low cell voltage, Angew. Chem. Int. Ed. 62 (2023) e202217601.
[17] C. Yan, Y. Liao, C. Shen, X. Weng, R. Lei, C. Liao, Y. Zhou, M. Wang, Uranium extraction by a graphene-based asymmetric electrode configuration through combined complexation, electro-adsorption, and photocatalytic reduction, Chem. Eng. J. 461 (2023) 142012.
[18] H. Yang, X. Liu, M. Hao, Y. Xie, X. Wang, H. Tian, G.I.N. Waterhouse, P.E. Kruger, S.G. Telfer, S. Ma, Functionalized iron-nitrogen-carbon electrocatalyst provides a reversible electron transfer platform for efficient uranium extraction from seawater, Adv. Mater. 33 (2021) 2106621.
[19] H. Ye, T. Li, Y. Huang, J. Jin, J. Fei, M. Wu, J. Yao, Amyloid-like coatings decorated electrodes boost the uranium electro-adsorption from seawater, Chem. Eng. J. 451 (2023) 138615.
[20] L. Zhou, J. Lian, Q. Li, J. Li, Y. Shao, G. Wu, T. Ding, X. Cui, T. Chen, W. Zhu, Unveiling the critical role of surface hydroxyl groups for electro-assisted uranium extraction from wastewater, Inorg. Chem. 62 (2023) 21518–21527.
[21] Y. Liao, R. Lei, X. Weng, C. Yan, J. Fu, G. Wei, C. Zhang, M. Wang, H. Wang, Uranium capture by a layered 2D/2D niobium phosphate/holey graphene architecture via an electro-adsorption and electrocatalytic reduction coupling process, J. Hazard. Mater. 442 (2023) 130054.
[22] Y. Chen, X. Yin, N. Zheng, Z. Lin, T. Fujita, S. Ning, Y. Chen, X. Wang, Flexible self-supporting $Na_3MnTi(PO_4)_3$@C fibers for uranium extraction from seawater by electro sorption, J. Hazard. Mater. 461 (2024) 132664.
[23] W. Wang, Q. Luo, L. Li, Y. Wang, X. Huo, S. Chen, X. Du, Ni. Wang, Ni-single-atom mediated 2D heterostructures for highly efficient uranyl photoreduction, Adv. Funct. Mater. 33 (2023) 2302913.
[24] Y. Li, G. Zou, S. Yang, Z. Wang, T. Chen, X. Yu, Q. Guo, R. He, T. Duan, W. Zhu, Integration of bio-inspired adsorption and photodegradation for the treatment of organics-containing radioactive wastewater, Chem. Eng. J. 364 (2019) 139–145.
[25] X. Gong, L. Tang, R. Wang, Z. Guo, P. Huang, L. Zhou, J. Zou, J. Lei, H. Liu, N. Li, X. Tang, W. Zhu, R. He, Achieving efficient photocatalytic uranium extraction within a record short period of 3 min by up-conversion erbium doped ZnO nanosheets, Chem. Eng. J. 450 (2022) 138044.
[26] H. Li, F. Zhai, D. Gui, X. Wang, C. Wu, D. Zhang, X. Dai, H. Deng, X. Su, J. Diwu, Z. Lin, Z. Chai, S. Wang, Powerful uranium extraction strategy with combined ligand complexation and photocatalytic reduction by postsynthetically modified photoactive metal-organic frameworks, Appl. Catal. B Environ. 254 (2019) 47–54.
[27] M. Xie, Y. Shen, W. Ma, D. Wei, B. Zhang, Z. Wang, Y. Wang, Q. Zhang, S. Xie, C. Wang, Y. Wang, Fast screening for copper-based bimetallic electrocatalysts: efficient electrocatalytic reduction of CO_2 to C_{2+} products on magnesium-modified copper, Angew. Chem. Int. Ed. 61 (2022) e202213423.
[28] Y. Xin, K. Yu, L. Zhang, Y. Yang, H. Yuan, H. Li, L. Wang, J. Zeng, Copper-based plasmonic catalysis: recent advances and future perspectives, Adv. Mater. 33 (2021) 2008145.
[29] Y. Sun, Z. Yao, Q. Lei, Y. Zhao, Z. Ren, W. Zhang, J. Si, L. Zhang, W. Wen, D. Zhu, X. Li, R. Tai, Ultrahigh-speed aqueous copper electrodes stabilized by phosphorylated interphase, Adv. Mater. 35 (2023) 2305087.
[30] C. Lin, J. Chen, Z. Wu, R. Chi, H. Lin, Y. Lv, X. Ye, W. Luo, Phosphate-functionalized fibrous adsorbent for effectively extracting uranium from seawater, Ind. Eng. Chem. Res. 61 (2022) 2227–2236.
[31] T. Zhu, Q. Chen, P. Liao, W. Duan, S. Liang, Z. Yan, C. Feng, Single-atom Cu catalysts for enhanced electrocatalytic nitrate reduction with significant alleviation of nitrite production, Small 16 (2020) 2004526.
[32] S. Zhou, J. Wang, J. Li, L. Fan, Z. Liu, J. Shi, W. Cai, Surface-growing organophosphorus layer on layered double hydroxides enables boosted and durable electrochemical freshwater/seawater oxidation, Appl. Catal. B Environ. 332 (2023) 122749.
[33] Y. Peng, Y. Zhang, Q. Tan, H. Huang, Bioinspired construction of uranium ion trap with abundant phosphate functional groups, ACS Appl. Mater. Interfaces 13 (2021) 27049–27056.
[34] Y. Tian, L. Liu, F. Ma, X. Zhu, H. Dong, C. Zhang, F. Zhao, Synthesis of phosphorylated hyper-cross-linked polymers and their efficient uranium adsorption in water, J. Hazard. Mater. 419 (2021) 126538.
[35] Y. Liao, M. Wang, D. Chen, Electrosorption of uranium(VI) by highly porous phosphate-functionalized graphene hydrogel, Appl. Surf. Sci. 484 (2019) 83–96.
[36] J. Chang, Q. Bao, C. Zhang, X. Zhao, Z. Cao, Y. Wang, R. Li, R. Guo, H. Li, J. He, P. Pan, Z. Yang, J. Wei, Rapid preparation and photocatalytic properties of octahedral Cu_2O@Cu powders, Adv. Powder Technol. 13 (2021) 27049–27056.
[37] J. Gao, A. Bahmanpour, O. Kröcher, S. Zakeeruddin, D. Ren, M. Grätzel, Electrochemical synthesis of propylene from carbon dioxide on copper nanocrystals, Nat. Chem. 15 (2023) 705–713.
[38] H. Zhu, J. Hu, Z. Zhang, Z. Zhuang, J. Hao, F. Duan, S. Lu, X. Wang, M. Du, Lewis acid sites incorporation promotes CO_2 electroreduction to multicarbon oxygenates over B-CuO nanotubes, Appl. Catal. B Environ. 339 (2023) 123082.
[39] X. Liu, Y. Yin, K. Xiong, M. Li, Facile synthesis of low-cost Fe_3C-nitrogen and phosphorus co-doped porous carbon nanofibers: the efficient hydrogen evolution reaction catalysts, J. Alloy. Compd. 856 (2021) 156213.
[40] K. Jiang, Y. Huang, G. Zeng, F. Toma, W. Goddard, A. Bell, Effects of surface roughness on the electrochemical reduction of CO_2 over Cu, ACS Energy Lett. 5 (2020) 1206–1214.
[41] Y. Yang, I. Roh, S. Louisia, C. Chen, J. Jin, S. Yu, M. Salmeron, C. Wang, P. Yang, Operando resonant soft x-ray scattering studies of chemical environment and interparticle dynamics of Cu nanocatalysts for CO_2 electroreduction, J. Am. Chem. Soc. 144 (2022) 8927–8931.
[42] Z. Zhang, Z. Wang, K. An, J. Wang, S. Zhang, P. Song, Y. Bando, Y. Yamauchi, Y. Liu, Ti^{3+} tuning the ratio of Cu^{+}/Cu^{0} in the ultrafine Cu nanoparticles for boosting the hydrogenation reaction, Small 17 (2021) 2008052.

[43] S. Lv, M. Li, X. Wu, X. Zhang, Y. Hua, L. Bi, Q. Fang, T. Cai, A non-polluting method for rapidly purifying uranium-containing wastewater and efficiently recovering uranium through electrochemical mineralization and oxidative roasting, J. Hazard. Mater. 416 (2021) 125885.
[44] Z. Gao, S. Chen, H. Ding, Y. Song, Z. Li, H. Wang, H. Wu, H. Li, Y. Su, Experimental study on efficient electrocatalytic reduction of U(VI) at amine-amidoxime bifunctional graphite felt electrode, Inorg. Chem. Commun. 146 (2022) 110134.
[45] L. Feng, H. Wang, T. Feng, B. Yan, Q. Yu, J. Zhang, Z. Guo, Y. Yuan, C. Ma, T. Liu, N. Wang, In situ synthesis of uranyl-imprinted nanocage for selective uranium recovery from seawater, Angew. Chem. Int. Ed. 61 (2022) e202101015.
[46] X. Xu, L. Xu, J. Ao, Y. Liang, C. Li, Y. Wang, C. Huang, F. Ye, Q. Li, X. Guo, J. Li, H. Wang, S. Ma, H. Ma, Ultrahigh and economical uranium extraction from seawater via interconnected open-pore architecture poly(amidoxime) fiber, J. Mater. Chem. A 8 (2020) 22032–22044.
[47] H. Li, N. He, C. Cheng, H. Dong, J. Wen, X. Wang, Antimicrobial polymer contained adsorbent: a promising candidate with remarkable anti-biofouling ability and durability for enhanced uranium extraction from seawater, Chem. Eng. J. 388 (2020) 124273.
[48] S. Shi, Y. Qian, P. Mei, Y. Yuan, N. Jia, M. Dong, J. Fan, Z. Guo, N. Wang, Robust flexible poly(amidoxime) porous network membranes for highly efficient uranium extraction from seawater, Nano Energy 71 (2020) 104629.
[49] W. Sun, L. Feng, J. Zhang, K. Lin, H. Wang, B. Yan, T. Feng, M. Cao, T. Liu, Y. Yuan, N. Wang, Amidoxime group-anchored single cobalt atoms for anti-biofouling during uranium extraction from seawater, Adv. Sci. 9 (2022) 2105008.
[50] Y. Wang, Z. Lin, Q. Liu, J. Zhu, J. Liu, J. Yu, R. Chen, P. Liu, J. Wang, Simple one-step synthesis of woven amidoximated natural material bamboo strips for uranium extraction from seawater, Chem. Eng. J. 425 (2021) 131538.
[51] S. Feng, L. Feng, M. Wang, Y. Yuan, Q. Yu, T. Feng, M. Cao, N. Wang, Q. Peng, Highly efficient extraction of uranium from seawater by natural marine crab carapace, Chem. Eng. J. 430 (2022) 133038.
[52] C. Huang, L. Xu, X. Xu, L. Ma, H. Bao, J. Liao, J. Wang, J. Han, G. Xu, D. Huang, B. Ye, H. Zhang, M. Wu, X. Zhao, H. Ma, Highly amidoxime utilization ratio of porous poly (cyclic imide dioxime) nanofiber for effective uranium extraction from seawater, Chem. Eng. J. 443 (2022) 136312.
[53] T. Liu, R. Zhang, M. Chen, Y. Liu, Z. Xie, S. Tang, Y. Yuan, N. Wang, Vertically aligned polyamidoxime/graphene oxide hybrid sheets' membrane for ultrafast and selective extraction of uranium from seawater, Adv. Funct. Mater. 32 (2022) 2111049.
[54] Z. Wang, R. Ma, Q. Meng, Y. Yang, X. Ma, X. Ruan, Y. Yuan, G. Zhu, Constructing uranyl-specific nanofluidic channels for unipolar ionic transport to realize ultrafast uranium extraction, J. Am. Chem. Soc. 143 (2021) 14523–14529.
[55] Z. Wang, Q. Meng, R. Ma, Z. Wang, Y. Yang, H. Sha, X. Ma, X. Ruan, X. Zou, Y. Yuan, G. Zhu, Constructing an ion pathway for uranium extraction from seawater, Chem 6 (2020) 1683–1691.
[56] B. Yan, C. Ma, J. Gao, Y. Yuan, N. Wang, An ion-crosslinked supramolecular hydrogel for ultrahigh and fast uranium recovery from seawater, Adv. Mater. 32 (2020) 1906615.
[57] S. Zhao, Y. Yuan, Q. Yu, B. Niu, J. Liao, Z. Guo, N. Wang, A dual-surface amidoximated halloysite nanotube for high-efficiency economical uranium extraction from seawater, Angew. Chem. Int. Ed. 58 (2019) 14979–14985.
[58] R. Tian, J. Wang, Y. Sun, W. Zhang, Y. Liu, Synergistic mechanism of B doping and NiO loading on the excellent PEC performance and high stability of TiO_2 nanotube photoanodes, J. Catal. 426 (2023) 178–188.
[59] Y. Gao, S. Qian, H. Wang, W. Yuan, Y. Fan, N. Cheng, H. Xue, T. Jiang, J. Tian, Boron-doping on the surface mediated low-valence Co centers in cobalt phosphide for improved electrocatalytic hydrogen evolution, Appl. Catal. B Environ. 320 (2023) 122014.